Eur. Phys. J. E **14**, 395–404 (2004)
DOI 10.1140/epje/i2004-10021-5

THE EUROPEAN PHYSICAL JOURNAL E

Vibrated sessile drops: Transition between pinned and mobile contact line oscillations

X. Noblin[a], A. Buguin, and F. Brochard-Wyart[b]

Physico-Chimie Curie, UMR 168 Institut Curie / CNRS, 11 rue Pierre et Marie Curie 75231 Cedex 05 Paris, France

Received 4 April 2004 /
Published online: 10 August 2004 –

Abstract. We study the effects of vertical vibrations on non-wetting large water sessile drops flattened by gravity. The solid substrate is characterized by a finite contact angle hysteresis (10–15 degrees). By varying the frequency and the amplitude of the vertical displacement, we observe two types of oscillations. At low amplitude, the contact line remains pinned and the drop presents eigen modes at different resonance frequencies. At higher amplitude, the contact line moves: it remains circular but its radius oscillates at the excitation frequency. The transition between these two regimes arises when the variations of contact angle exceed the contact angle hysteresis. We interpret different features of these oscillations, such as the decrease of the resonance frequencies at larger vibration amplitudes. The hysteresis acts as "solid" friction on the contour oscillations, and gives rise to a stick-slip regime at intermediate amplitude.

PACS. 47.55.Dz Drops and bubbles – 68.08.Bc Wetting – 47.35.+i Hydrodynamic waves

1 Introduction

We focus on forced oscillations of water sessile drops lying on a flat substrate characterized by a moderate contact angle hysteresis defined as the difference between the *cosinus* of receding and advancing contact angles $H = \cos(\theta_r) - \cos(\theta_a)$. The drops are flattened by gravity and the substrate is vertically vibrated with a loudspeaker. Depending on frequency and amplitude, we observe two regimes of axisymmetric oscillations for the drop: Type I, where the contact line remains fixed and Type II, where the contact line oscillates. The first modes occur at low amplitude, whereas Type-II modes appear above a threshold amplitude.

Oscillations of supported drops and inertial contact line dynamics raise fundamental questions and have practical applications. The oscillations of spherical liquid drops have been studied for more than a century by Kelvin, Rayleigh, Lamb [1]... Less works concern the case of sessile drops on a solid support. The first experimental [2] and theoretical [3] studies were motivated to understand the influence of liquid drop vibrations on crystal growth in microgravity. Different studies followed [4–9] with several practical and scientific applications such as dynamic surface tension measurements (see [10] and references therein) and droplet ejection [11–13]. Oscillations of drops with a solid support are also related to their impacts [14,15] and rebounds [16,17] on the surface, with applications ranging from herbicide and insecticide deposition to inkjet printing and microvolume deposition. Most studies of supported drop oscillations concern fixed contact line conditions or no contact line at all, for example for air-levitating drops [18]. In [6,7], the hysteresis of the substrate is not characterized and no particular attention is given to differentiate between modes I and II. The only work which treats the case of two kinds of modes is a numerical study [19] with the two idealized cases of fixed contact line (Type I) and fixed contact angle with free contact line (what we will call later "pure Type II"). Our study is the first experimental work investigating the effect of hysteresis on supported drop oscillations leading to stick slip motion of the triple line. Varying frequency and amplitude, we are able to observe the two types of modes with the same system. Another aim of our work is to provide a simple model to estimate the resonance frequencies for the Type-I and pure-Type-II modes based on stationary wave conditions for capillary-gravity waves.

Another aspect concerns the fast dynamics of contact lines. Many studies focus on viscous liquids with applications in liquid coatings, paint deposition, spraying of herbicides or insecticides... Much less work deals with the inertial case and unsteady motion of the contact line. Oscillating motions of fibers or plates immersed in a liquid bath have been studied for both model and hysteretic substrates [20–22]: different motions of the contact line such as pure stick, stick-slip and pure slippage are described and are similar to those observed in our study. Our aim,

[a] e-mail: xavier.noblin@curie.fr.
[b] e-mail: Francoise.Brochard-Wyart@curie.fr.

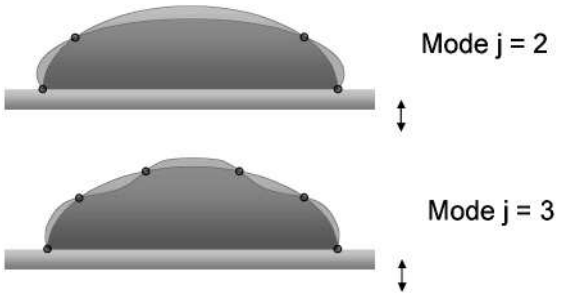

Fig. 1. Schematic representation of the drop profiles for the modes $j = 2$ (4 nodes) and $j = 3$ (6 nodes) (Nodes are emphasized with black spots).

here, is to study the inertial contact line motion for sessile vibrated drops, where the modes are discrete because the size of the drop is finite, and to focus on the role of hysteresis. As far as we know, this is the first study of the problem.

In Section 2, we study Type-I modes. We present the experimental setup. We measure the spectra of the eigen modes. We interpret our results as stationary capillary-gravity waves on the drop interface.

In Section 3, we study Type-II modes. We use another experimental setup to follow the contours of the drops. The resonance frequencies are compared to the frequencies of Type-I modes. We interpret the shift of eigen frequencies via a modification of boundary conditions. We observe carefully the variations of the contact angle and the contact line position during the vibration of the drop. A regime of stick slip is observed at intermediate amplitude: the hysteresis is analogous to a solid friction acting on the line.

2 Type-I modes: immobile contact line

A drop of volume V, lying on a polystyrene substrate is subjected to a low amplitude periodic acceleration of frequency f:

$$a = -(2\pi f)^2 u_0 \cos(2\pi f t),$$

where u_0 is the spatial displacement of the substrate.

We observed axisymmetric surface waves on the drop. The contact line remains pinned by the substrate due to wetting hysteresis. These oscillations are the superposition of eigen modes characterized by a number j. j is half the number of nodes along the drop profile (Fig. 1).

Each mode j has a resonance frequency f_j. By varying the excitation frequency f and the drop volume V, we were able to measure the resonance frequencies f_j for j ranging from 2 to 6.

2.1 Materials and methods

An ultra-pure water drop is deposited on a Petri dish (polystyrene) which is slightly concave to avoid the escape of drops at high-amplitude vibrations. We measure the receding and advancing contact angles for the air/water/polystyrene system (see Tab. 1).

Table 1. Advancing and receding contact angles.

θ_a	θ_r	$\Delta\theta = \theta_a - \theta_r$
$92 \pm 1°$	$78.5 \pm 1°$	$13.5 \pm 2°$

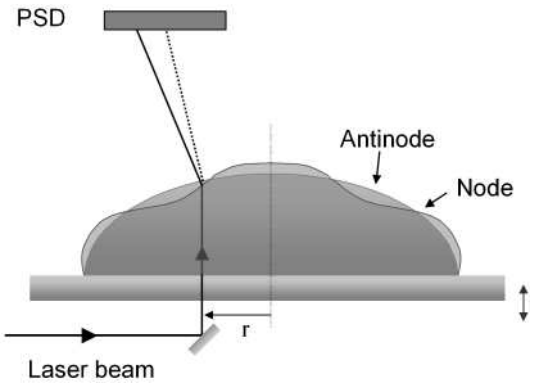

Fig. 2. Schematic representation of the experimental setup: the laser beam deflection at the air/water interface gives the local slope of the drop at distance r from its center.

A loudspeaker is used to vibrate the substrate (maximum peak-to-peak displacement 14 mm). It is linked to a power amplifier connected to a digital function generator or an Input/Output (I/O) computer board.

The vertical displacement of the substrate is measured by the deflection of a laser beam (from a mirror fixed on the moving part of the loudspeaker) using a Position-Sensitive Detector (PSD) also connected to the I/O card (Fig. 2). A program (Labview) measures simultaneously the frequency and the acceleration with a 10 kHz acquisition rate.

The substrate is bound up with the moving part of the loudspeaker. To avoid evaporation and contamination effects, it is placed in a closed vessel with an optical window. Water drops with a volume ranging from 0.1 ml to 3 ml are deposited on the substrate.

We follow the fluctuations of the drop by looking at the local variations of the air/water interface slope. A vertical laser beam goes through the drop at a distance r from its center, is refracted at the liquid/air interface and its deflection is measured using a PSD. For each value of the radius r, we performed angle response measurement as a function of frequency.

The experimental procedure is repeated for many drops of increasing volume. Our aim is to determine the relative amplitude of each mode j as a function of r. For $r = 0$, the amplitude of all modes is zero. Two excitation signals are used to probe the response of the drop. First, we use a pure sinusoidal excitation. By varying the frequency at constant acceleration and measuring the response amplitude, we obtain a frequency response spectrum. In a second type of experiment, we send to the loudspeaker a white noise signal. We perform a Fourier transform of the response signal. We normalize it by the measured acceleration spectra. The time required to have the same resolution as for a pure sinusoidal signal is

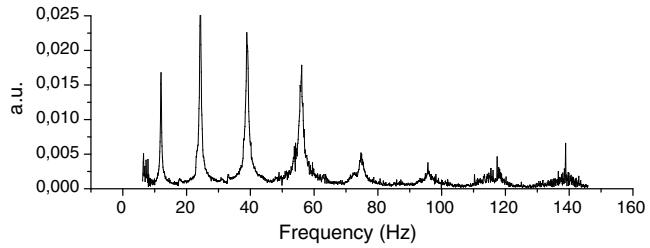

Fig. 3. Normalized response spectra: air/water interface slope oscillations for the drop at a distance $r = 1.5\,\mathrm{mm}$ from its center ($V = 1\,\mathrm{mL}$).

significantly reduced. We focused on resonance frequencies values and not on precise amplitude measurements.

Special care is devoted to the deposition of drops before each measurement. Due to the wetting hysteresis, the contact angle after drop deposition ranges between $[\theta_\mathrm{r}, \theta_\mathrm{a}]$. To work in well-defined conditions, we start our measurements from the mean equilibrium angle θ_E. By vibrating the drop at high amplitude and a well-chosen frequency, as we will see in Section 3, we put the contact line into periodic motion. The contact angle reaches a mean value θ_E. We verify that $\cos(\theta_\mathrm{E}) = (\cos\theta_\mathrm{r} + \cos\theta_\mathrm{a})/2$, in agreement with previous studies when the surface is smooth; this is not always true on rough surfaces [23–25]. By reducing the excitation amplitude, we return to a pinned contact line situation and we can begin the measurements with a contact angle value at rest equal to θ_E.

2.2 Spectra

We measure slope response spectra for twelve drop volumes ranging from 0.1 mL to 3 mL (with corresponding radius ranges from 4.2 mm to 17.6 mm). The drops are increasingly flattened by gravity (capillary length $\kappa^{-1} = 2.7\,\mathrm{mm}$). We present an example of such spectra on Figure 3.

We note that the $j = 2$ peak has a relative low amplitude compared to the other modes. As mentioned in Section 2.1, it is simply due to the particular location of the laser beam from the drop center.

We measure different spectra for different values of r. We verify that the peak positions remain unchanged, only their relative amplitudes vary. We present in Figure 4 a superposition of the different spectra obtained with increasing values of r. We note that the maximum amplitude of each mode decreases when mode number increases.

2.3 Resonance frequencies

The log-log plot of resonance frequencies as a function of drop volume V is shown in Figure 5. We see that frequencies increase with mode number and decrease with drop volume. The exponent of the power fit increases from 0.45 to 0.53 with mode number going from $j = 2$ to $j = 6$. These fits are empirical guides, we only expect a true power law in the limit of pure capillary and gravity

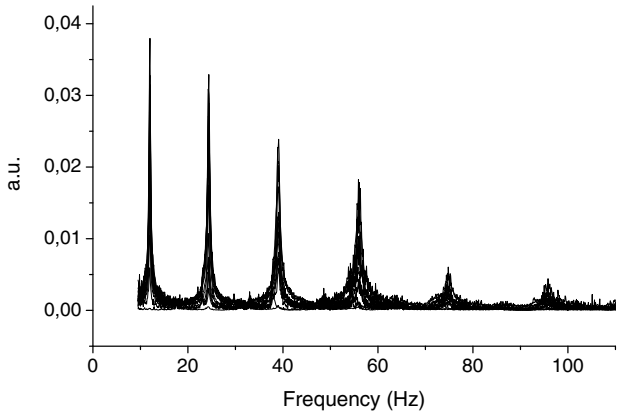

Fig. 4. Superposition of spectra obtained at 8 different positions of the laser beam from the center of the drop for r ranging from 0 to 6.5 mm ($V = 1\,\mathrm{mL}$).

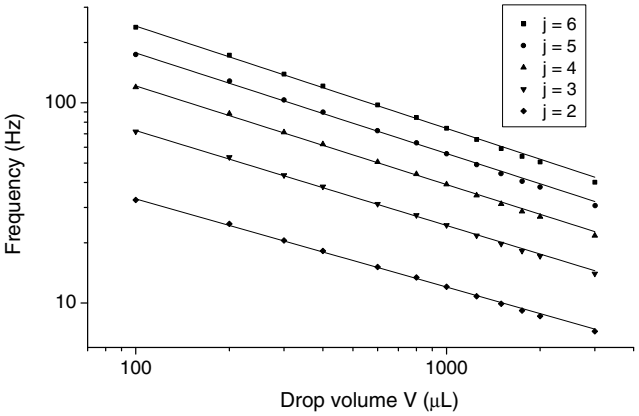

Fig. 5. Log-log representation of the resonance frequencies *versus* drop volume. The variations are well described by a power law with an exponent close to 0.5, it increases from 0.45 for $j = 2$ to 0.53 for $j = 6$ (straight lines).

regimes (for both of them, as we will see later $f \propto V^{0.5}$ for a given mode). In the cross-over region the relation is more complex but it is not surprising to find an exponent close to 0.5.

2.4 Interpretation

The different modes are stationary surface waves. The nontrivial equilibrium shape of the drop leads to a complicated three-dimensional wave pattern. An analytical description can be obtained only in the capillary regime assuming that the drop is in partial contact with a spherical substrate [3]. Complex numerical simulations are needed to solve the problem with gravity [10] and no analytical expression is available to calculate the resonance frequencies. To simplify the problem, we consider the waves as one dimensional. We calculate pseudo wave vector values $q_j(V)$ for each mode number and drop size. From the dispersion relation of capillary-gravity waves, we obtain approximate theoretical values for the eigen frequencies, which are compared to the resonance frequencies measured.

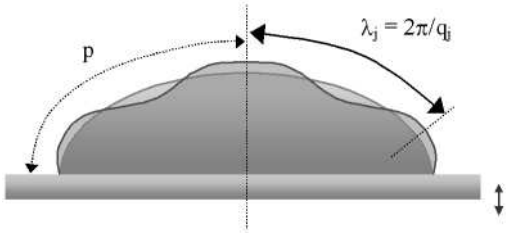

Fig. 6. Pseudo wavelength for mode $j = 3$.

To calculate the pseudo wavelengths $\lambda_j = \frac{2\pi}{q_j}$, we write that it is the mean distance between two consecutive nodes along the drop profile. With p the arc length of the meridian curve from the center to the edge of the drop at equilibrium (see Fig. 6), we find the relation $(j-1/2)\lambda_j = 2p$. Then

$$q_j = \frac{2\pi}{\lambda_j} = \frac{\pi(j-1/2)}{p}\,. \tag{1}$$

For a sessile drop at equilibrium, p depends on drop volume and contact angle, taken at its equilibrium value $\theta_{\mathrm{E}} = 85°$ for our system. No analytical expression exists in the general case, so we calculated numerically various exact drop profiles and deduced the values of p as a function of the drop volume. We finally deduced the pseudo wave vector values q_j for each mode.

In our experimental conditions, inertia dominates viscosity effects. The Reynolds number, calculated with the phase velocity and the wavelength, has characteristic values between 100 and 1000. For small oscillations the modes are decoupled and present a linear behavior. Hence, we observed a common resonance phenomenon for each mode when the excitation frequency is close to its natural frequency. For 1D capillary-gravity waves on a liquid bath of depth h with wave vector q, we have [26]

$$\omega^2 = \left(gq + \frac{\gamma}{\rho}q^3\right)\tanh\left(qh\right)\,. \tag{2}$$

We used for q the values given by the approximate relation equation (1).

For the depth h, we take the mean height of the drop profile h_{m}, defined by

$$h_{\mathrm{m}} = \frac{V}{\pi R^2}\,. \tag{3}$$

We then obtain

$$\omega_j^2 = \left(gq_j + \frac{\gamma}{\rho}q_j^3\right)\tanh\left(q_j\frac{V}{\pi R^2}\right)\,. \tag{4}$$

We compare in Table 2 experimental results and calculated values with our 1D model for two different drop volumes. We took $\gamma = 72.8\,\mathrm{mN\cdot m^{-1}}$, $\rho = 998\,\mathrm{kg\cdot m^{-3}}$ and $g = 9.81\,\mathrm{m\cdot s^{-2}}$. We note a good agreement, except for the mode $j = 1$ where our model is more approximate.

We plot the resonance frequencies as a function of q on a log-log plot (Fig. 7). We show in the graph the slopes 3/2 and 1 corresponding to capillary and gravity regimes,

Table 2. Comparison of the resonance frequencies (in Hz) between the model and the experiment ($V = 0.1\,\mathrm{mL}$, and $V = 2\,\mathrm{mL}$).

Mode number j	$V = 0.1$ mL		$V = 2$ mL	
	Exp.	Model	Exp.	Model
2	32.7	35.5	8.6	9.1
3	71.8	75.2	17.2	17.3
4	119.8	123.5	27.0	27.1
5	174.7	178.9	38.1	38.1
6	238.6	240.9	50.7	50.4

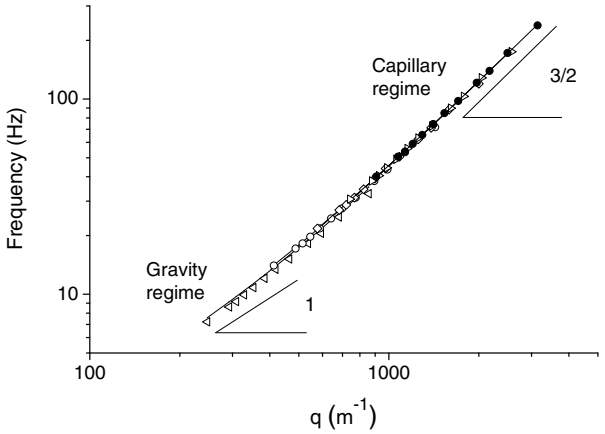

Fig. 7. Log-log representation of the resonance frequencies as a function of the wave vector. (◁) $j = 2$, (○) $j = 3$, (◇) $j = 4$, (▷) $j = 5$ and (●) $j = 6$. The straight line represents calculated values of the model. Drop volumes vary from 0.1 mL to 3 mL.

respectively. The straight line is the calculated value of our simple model.

All the frequencies fall quantitatively on a master curve on Figure 7. The model for the wave vectors is satisfactory in the range of drop sizes and frequencies we explore.

Another important point is the synchronous response of the drop: the response frequency is the same as the excitation one. This is not the case in the Faraday experiment, where a filled recipient of water is vibrated, and subharmonic bulk surface waves are observed (often independently of edges constraints). In our experimental situation, the modes are stationary waves strongly induced by edges conditions. The meniscus emits waves towards the drop center, which interfere constructively at resonance; this is not a bulk behavior of a fluid interface.

We did not observe remarkable nonlinear behavior, owing to the low amplitude of the oscillations.

3 Type-II modes: mobile contact line

At low excitation amplitude, we have seen that the contact line remains pinned by the substrate and the contact angle is oscillating (Type I). For higher excitation amplitudes, the contact angle variations can exceed the contact angle

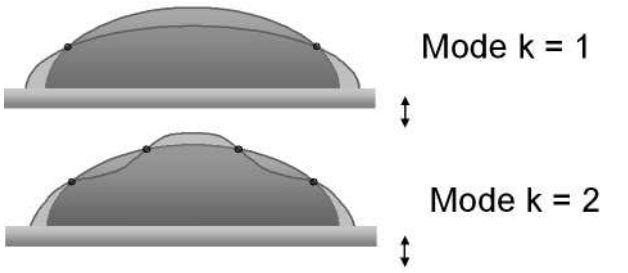

Fig. 8. Modes $k = 1$ (2 nodes) and $k = 2$ (4 nodes); nodes are emphasized with black spots.

hysteresis, and the contact line can be put into oscillatory motion (Type-II modes).

On a perfect substrate, with no hysteresis and no viscous dissipation, we would observe pure-Type-II modes with a condition of constant contact angle $\theta = \theta_{\mathrm{E}}$ as studied numerically in [19]. The same conditions apply for the general inertial contact line motion [27]. With this condition, the number of wavelengths along the whole meridian curve would be diminished by 1/2 (See Fig. 8). As for the Type-I modes for which we used j number, we characterize these modes with the number k, which is half the number of nodes along the drop (see Fig. 8). We then have the new relation: $k\lambda_k = 2p$ instead of $(j - 1/2)\lambda_j = 2p$.

In our case, with hysteretic substrates, we observe oscillations of the drop radius at excitation frequency coupled to oscillations of the contact angle. We cannot restrict the motion to a simple condition of constant contact angle. We will keep the number k to characterize all the oscillations with a moving contact line although they are not pure modes.

3.1 Experimental setup

To have a better understanding of the phenomena, we use different complementary methods to study these modes. In the following, we present the kind of information they provide, their advantages and drawbacks. One of the problems encountered is how to differentiate between the real contact line position and the position of the maximum radius of the drop projection for contact angles larger than 90°. We then detail the experimental procedure.

The first method, using a laser line, gives a local value of the instantaneous radius of the drop $R(t)$. A laser line is projected vertically on the drop along the radial direction, with a part on the substrate, and a part on the drop, (see Fig. 9). The rays that fall on the substrate are reflected by a mirror underneath then by a beam splitter and are collected by a photodiode. The rays that fall on the drop, close to the contact line are reflected or refracted by the interface and are not collected by the photodiode.

If the intensity is uniform along the laser line, the intensity on the photodiode is proportional to the position of the contact line. This is true if the contact angle is less than 90°. When the contact angle is greater than 90°, we measure the maximum position of the projection of the drop on the substrate and not the real

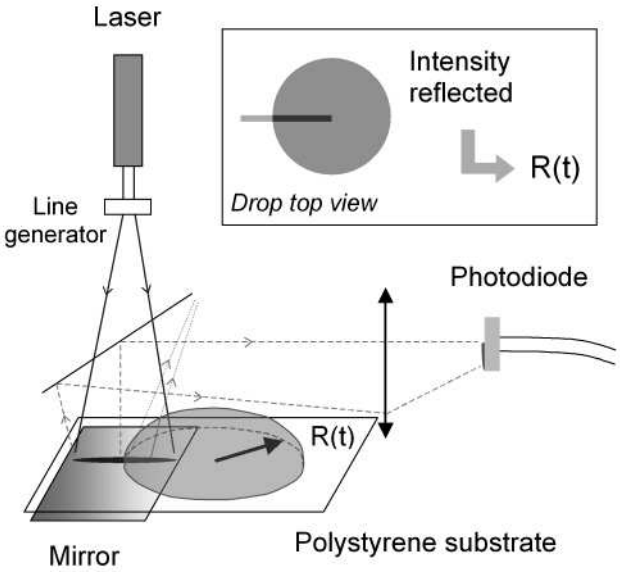

Fig. 9. Experimental setup: observation of the local radius variation with a laser line.

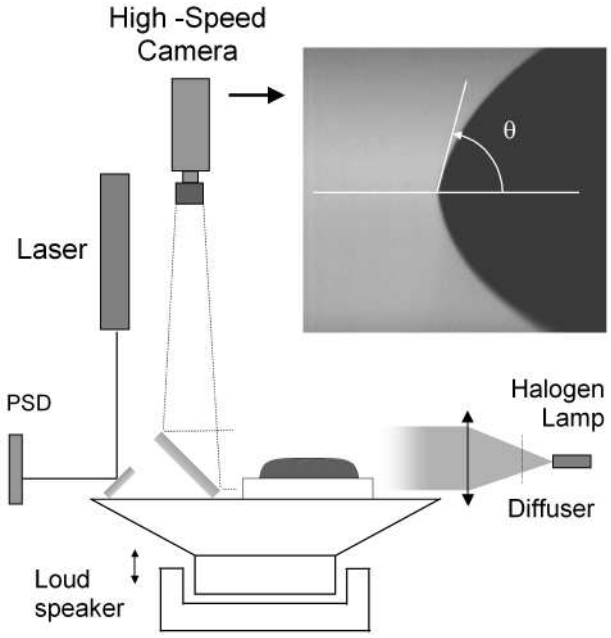

Fig. 10. Experimental setup for side-view drop visualization during vibrations. In the lower part of the image, we see the reflected image of the drop on the substrate. The angle of observation is 3°.

contact line position. For large contact angle values, we have discrepancies between the two quantities. A large variation of the contact angle could be seen as a contact line oscillation although it is pinned. This effect can be misleading around the transition between the two types of modes, where the amplitude of radius oscillations is small. This method, which gives local information, is not applicable for very large contact angles but has high temporal resolution (tens of kHz). One advantage is the possibility to vary successively amplitude or frequency

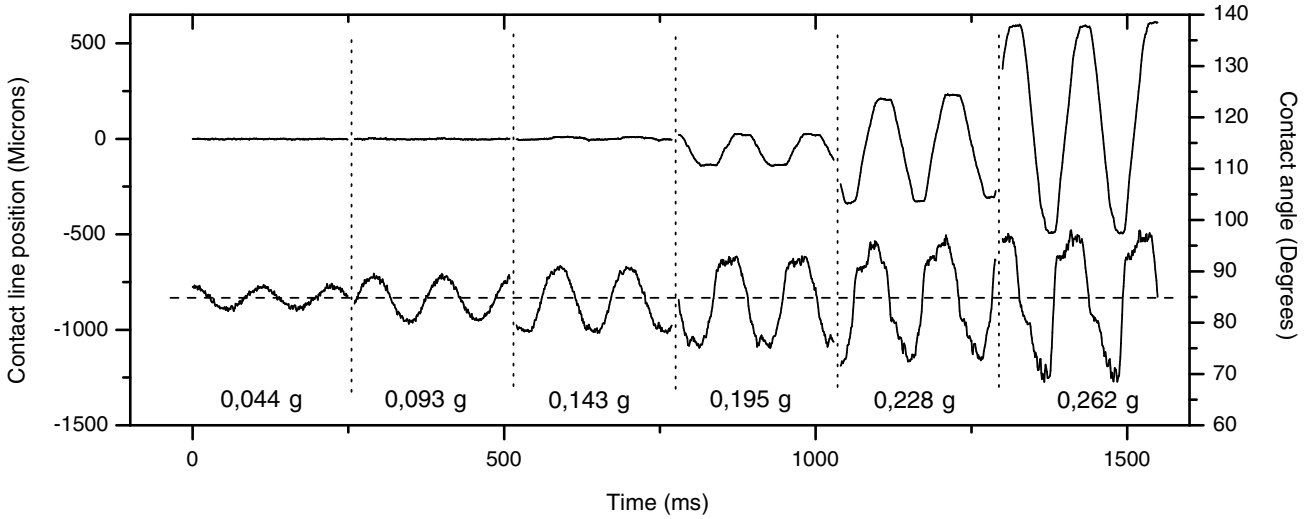

Fig. 11. Transition between stick and stick-slip motions of the contour. Lower curves are contact angle (degrees) variations *versus* time, the dashed line represents θ_{E}. Higher curves are the contact line position (microns) around the starting position before vibrations. The six curves for different acceleration amplitudes are joined together in the same plot for comparison. $f = 9\,\mathrm{Hz}$, $V = 1\,\mathrm{mL}$.

with a programmed excitation and to measure different points in an automated way.

The second method uses a fast camera (up to 1000 image/s) in two ways: i) From *above*, it gives the coordinates of the contact line contour for each frame of a movie, then the mean radius of the drop as a function of time. We have global information. As for the laser method, we measure the radius of the projected image of the drop. ii) From a *side view* using an inclined mirror on the moving part of the loudspeaker, we keep the camera along the vertical axis, and the image of the substrate is then fixed in the field of view. The axis of view is slightly tilted (3° above horizontal): we see the drop profile and its reflection on the substrate (see Fig. 10).

By image analysis, the edge profile of the drop close to the contact line is determined. The program calculates the baseline position and a polynomial fit of the profile gives the contact angle value and the real contact line position. Even for contact angles larger than 90°, there is no vertical projection effect. The main drawback of this method is the time required to make a measurement compared to the laser method.

Due to the high amplitude of excitation and complex motion of the contact line, the phenomena studied are nonlinear, hence we did not use a noise excitation and Fourier transform method. We vary frequency $f = \omega/2\pi$ and acceleration amplitude a_0 of a pure sinusoidal signal. We perform two types of measurements to explore the (f, a_0)-space: i) Constant frequency to obtain transition curves between Type I and Type II as acceleration is increased. We use the camera method (side view). ii) Constant acceleration, to obtain frequency response spectra. We use the laser line method in an automated way. The camera method (top view) allows us to check that drops remain circular during oscillations and is used for qualitative observation.

3.2 Results

3.2.1 Threshold curves

We mainly look at the first mode (transition between $j = 2$ to $k = 1$) because of its higher amplitude. There are no particular differences for higher modes. We look at the contact angle and contact line position variations with the side-view camera method. The frequency is constant and acceleration is increased (Fig. 11). At low amplitude, the contact line is completely stuck by the substrate. We clearly see that when the contact angle variation exceeds the contact angle hysteresis, the contact line starts to move (the transition is close to the third curve, for 0.143 g). At higher excitation, the amplitudes of radius oscillations rapidly increase, the contact angle variations also increase and are no longer sinusoidal. From the radius variations we clearly see a stick-slip behavior: the contact line is pinned during a part of the time, then it advances (slip), stops for a while (stick), goes back (slip) and so on. The higher the excitation amplitude, the shorter the pinned time is. This behavior can be explained by the force of hysteresis, which acts as a "solid friction" on the moving line (as we will see in Sect. 3.3).

We have plotted for different frequencies (around the mode $k = 1$) curves of the amplitude of radius oscillation ΔR as a function of acceleration. When $\Delta R = 0$, we have only the Type-I modes. Above the transition, $\Delta R > 0$, we observe the Type-II modes.

We notice that the curve's shape depends strongly on frequency. The resonance frequency of the pinned line mode for a 1 mL drop is 12 Hz. i) Close to this frequency and for low acceleration, the amplitude of Type-II modes is zero, then by increasing the acceleration, we see that we have a threshold with a slope break-up. Above this threshold we observe Type-II modes with increasing amplitude. It corresponds on Figure 12 to the 12 Hz curve.

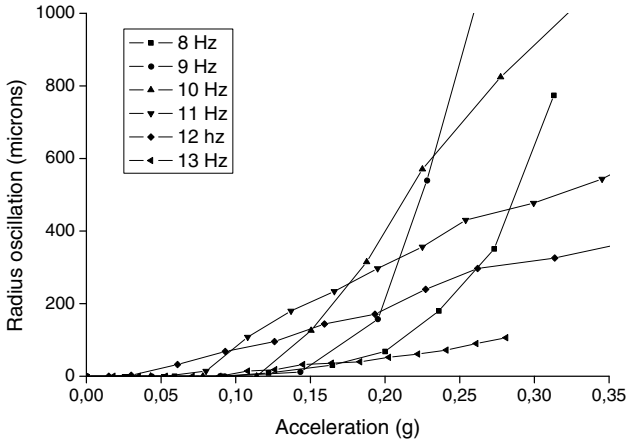

Fig. 12. Amplitude of radius oscillation *versus* acceleration for different frequencies, $V = 1\,\mathrm{mL}$.

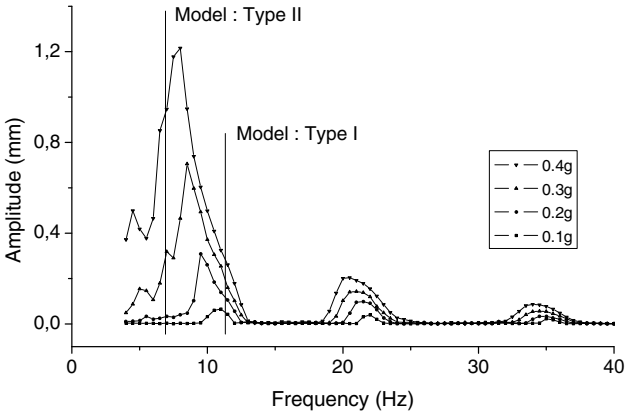

Fig. 13. Peak-to-peak oscillation of the radius in mm for a 1.25 mL drop ($R = 11.8$ mm) at constant acceleration (0.1 g to 0.4 g). The two vertical lines are the calculated values with our waves model for Type-I modes (11.35 Hz) and pure-Type-II modes (6.95 Hz).

ii) At lower frequencies, the transition is less abrupt and the slope is still increasing with acceleration in the range studied. The threshold acceleration value increases when the excitation frequency moves away from resonance of pinned modes: we need a higher excitation amplitude to observe the Type-II modes when the frequency is far from the resonance frequency of Type-I modes. Interestingly, for such lower frequencies, when we increase further excitation amplitude, the radius oscillation amplitude exceeds that of the higher-frequency curve.

3.2.2 Spectra

Instead of measuring ΔR as a function of acceleration at constant frequency, we also perform constant-acceleration measurements to obtain frequency response spectra as for pinned contact line modes in Section 2.2.

We observe in Figure 13 that at low acceleration amplitude, the contact line radius varies only for frequencies very close to the resonance frequencies of the pinned modes. Out of the resonance regions, the amplitude of the radius oscillation is strictly zero: the line is pinned by the substrate. At higher amplitude, the maximum radius oscillation amplitude increases and the width of the peaks increases too. We notice that, as for pinned contact line modes, the response amplitude decreases with mode number k.

We also clearly notice a shift towards low values for the frequencies of the peak's maxima. This decreasing in the resonance frequencies with amplitude is a classical features of non-harmonics oscillators, but it can have other origins. We explain it with the surface waves model using a different condition for the contact line which is no longer pinned, leading to smaller pseudo wave vectors, and thus smaller frequencies. We indicate in Figure 13 the resonance frequencies of Type-I and Type-II modes as calculated using the model discussed in the next section. We see that the complex modes we observed with a moving contact line draw nearer to the asymptotic limit of pure-Type-II modes at large fluctuation amplitude.

3.3 Interpretation

We have studied the dynamics of a vibrated sessile drop for which the contact line is moving. In the range of amplitude and frequency studied, this motion is axisymmetric. At low amplitude, the contact line remains pinned and the contact angle oscillates around its equilibrium value. When the excitation amplitude increases, the variation of the contact angle becomes larger than the contact angle hysteresis and the line is put into motion. For each drop size and excitation frequency, there is a threshold value of the excitation amplitude above which the contact line is put into motion. This motion is periodic at the excitation frequency as for the Type-I modes, but non-harmonic. Both the radius of the contact line and the contact angle are oscillating: we do not observe pure-Type-II modes, which can be seen only on model substrates with no hysteresis. Moreover, the contact line motion is complicated due to stick-slip behavior.

3.3.1 Frequency shift

To interpret the frequency shift, we used the same model of pseudo wave vector and surface waves as for Type-I modes, but with the limit condition of fixed contact angle (see Fig. 8). It leads to a new set of pseudo wave vectors and resonance frequency values. We have for the pseudo wavelengths: $k\lambda_k = 2p$, and the wave vectors:

$$q_k = \frac{\pi k}{p}\,. \tag{5}$$

A mode j corresponds to a mode $k = j - 1$, we then have: $q_k = \left(\frac{2k}{2k+1}\right) q_{j=k+1}$. We calculate the resonance frequencies using equation (2).

We found experimentally that with increasing amplitude, the frequencies of peak maxima are shifted toward low values. The resonance frequencies diminish and come close to the pure mode frequencies.

3.3.2 Oscillator with solid friction

The hysteresis opposes a constant resisting force on the moving line. The drop behaves like an oscillator with solid friction, ruled by the equation

$$\ddot{x} + \omega_k^2 x + \mu\, sgn\left(\dot{x}\right) = A\cos\left(\omega t\right)\,, \tag{6}$$

where μ is the solid friction coefficient, $sgn(u)$ is the function dependent on the sign of u: $u > 0 \Rightarrow sgn(u) = 1$ and $u < 0 \Rightarrow sgn(u) = -1$. ω_k is the natural frequency of the oscillator. Such systems have been studied in [28–30]. Authors found different possible motions depending on the ratio A/μ and ω/ω_k. At low forcing amplitude the oscillator is completely stuck, at higher amplitude, they observe stick-slip motion (with 2 stops by period or more) and also pure slipping oscillatory motion with no stops.

We observed in our experiments that under a threshold in excitation amplitude, the contact line remains pinned by the substrate. This is the first feature of solid friction related to the hysteresis H. Just above the threshold, during oscillations, the contact line remains pinned most of the time. The time of immobilization of the line decreases as the excitation amplitude increases. This is a second feature of forced solid friction oscillators. At much higher amplitude, we do not observe any stops and the contact line is always moving.

Our aim is now to derive equation (6) for the first mode ($k = 1$) in the simple case of large drops flattened by gravity (see [18,31]).

The total energy is the sum of gravitational energy $E_{\rm g}$, surface energy $E_{\rm s}$ and kinetic energy $E_{\rm c}$. Damping results from the work $L_{\rm s}$ of the solid friction force. The energy balance is

$$\frac{\mathrm{d}}{\mathrm{d}t}\left(E_{\rm g} + E_{\rm s} + E_{\rm c}\right) = -\frac{\mathrm{d}}{\mathrm{d}t}\left(L_{\rm s}\right)\,. \tag{7}$$

The gravity and surface term represent a potential energy $E = E_{\rm g} + E_{\rm s}$. Gravity tends to flatten the drop and surface energy to make it spherical and to reduce the drop radius. The final shape results from a minimum of potential energy at equilibrium. For the gravitational energy, we have simply: $E_{\rm g} = \rho V g z_{\rm m}$, with $z_{\rm m}$ the height of the center of mass. For surface energy, its varying part is: $E_{\rm s} = \gamma A_{\rm LV} + A_{\rm SL}\left(\gamma_{\rm SL} - \gamma_{\rm SV}\right)$ with $A_{\rm LV}$ and $A_{\rm SL}$ the Liquid/Vapor and Solid/Liquid interface area.

For small oscillations, and constant contact angle $\theta = \theta_{\rm E}$, the potential has the general form

$$E = E_{\rm eq} + \frac{1}{2}\left[\frac{\mathrm{d}^2E}{\mathrm{d}R^2}\right]\left(R - R_{\rm eq}\right)^2 \tag{8}$$

which leads to the common oscillator equation after the kinetic-energy calculation. The exact calculation of $\frac{\mathrm{d}^2E}{\mathrm{d}R^2}$ is complex, but easy in the limit of very large drops ($R \gg \kappa^{-1}$). We can assume a cylindrical shape of radius R and height $h = \frac{V}{\pi R^2}$.

The drop center of mass is $z_{\rm m} = h/2$. Hence, the gravitational term is simply

$$E_{\rm g} = \frac{\rho g V^2}{2\pi R^2}\,. \tag{9}$$

For the surface term, we write: $A_{\rm LV} \approx A_{\rm SL} \approx \pi R^2$ and $S = \gamma_{\rm SV} - \left(\gamma_{\rm SL} + \gamma\right) = -\gamma\left(1 - \cos(\theta_{\rm E})\right)$ the spreading parameter. We have then

$$E_{\rm s} = -S\pi R^2 = \gamma\left(1 - \cos(\theta_{\rm E})\right)\pi R^2\,. \tag{10}$$

The potential is

$$E(R) = \gamma\left(1 - \cos(\theta_{\rm E})\right)\pi R^2 + \frac{\rho g V^2}{2\pi R^2}\,. \tag{11}$$

We can derive a resulting force

$$F(R) = -\frac{\partial E}{\partial R} = \gamma\left(1 - \cos(\theta_{\rm E})\right)2\pi R - \frac{\rho g V^2}{\pi R^3}\,. \tag{12}$$

The equilibrium radius is given by $F(R_{\rm eq}) = 0$. Then:

$$\frac{\rho g V^2}{\pi R^4} = 2\pi\gamma\left(1 - \cos(\theta_{\rm E})\right)\,, \tag{13}$$

which leads to $h_{\rm eq} = \frac{V}{\pi R_{\rm eq}^2} = 2\kappa^{-1}\sin\left(\frac{\theta_{\rm E}}{2}\right)$. We have

$$\left[\frac{\mathrm{d}^2E}{\mathrm{d}R^2}\right]_{R=R_{\rm eq}} = 8\pi\gamma(1 - \cos(\theta_{\rm E})) \tag{14}$$

and around equilibrium, the potential is

$$E(R) \simeq 3\gamma(1-\cos(\theta_{\rm E}))\pi R_{\rm eq}^2 + 4\pi\gamma(1-\cos(\theta_{\rm E}))(R-R_{\rm eq})^2\,. \tag{15}$$

For the kinetic energy, we assume simple flows. We denote v_r and v_z the radial and vertical velocity. The incompressibility equation $\mathrm{div}\,\overrightarrow{V} = 0$ leads to

$$\frac{1}{r}\frac{\partial}{\partial r}(r v_r) + \frac{\partial v_z}{\partial z} = 0\,. \tag{16}$$

Looking for simple solutions such as $v_r(r,t)$ and $v_z(z,t)$, we find $v_r = \frac{r}{R}\frac{\mathrm{d}R}{\mathrm{d}t}$ and $v_z = -\frac{2z}{R}\frac{\mathrm{d}R}{\mathrm{d}t}$. We obtain the kinetic-energy density

$$e_{\rm c} = \frac{1}{2}\frac{\rho}{R^2}\left(\frac{\mathrm{d}R}{\mathrm{d}t}\right)^2\left(r^2 + 4z^2\right)\,. \tag{17}$$

We have for the total kinetic energy in the large drop limit:

$$E_{\rm c} = \frac{1}{4}\rho V\left(\frac{\mathrm{d}R}{\mathrm{d}t}\right)^2\,. \tag{18}$$

We have $\cos\theta_{\rm E} = \left(\cos\theta_{\rm a} + \cos\theta_{\rm r}\right)/2$. Then $\cos\theta_{\rm E} - \cos\theta_{\rm a} = \cos\theta_{\rm r} - \cos\theta_{\rm E} = H/2$

The solid friction force by unit contact line length has the same absolute value during advancing and receding processes: $F = \frac{\gamma H}{2}$. The infinitesimal work done against this force is for small oscillations

$$\mathrm{d}L_{\rm s} = sgn(\mathrm{d}R)2\pi R\mathrm{d}R\frac{\gamma H}{2} \simeq sgn(\mathrm{d}R)2\pi R_{\rm eq}\mathrm{d}R\frac{\gamma H}{2}\,. \tag{19}$$

The derived energy balance (7) leads to a classical solid friction oscillator equation with $u = R - R_{\rm eq}$:

$$\ddot{u} + \omega_1^2 u + \mu sgn(\dot{u}) = 0 \tag{20}$$

with $\omega_1^2 = -\left(\frac{16\pi S}{\rho V}\right)$, $\mu = \frac{2\pi R_{\rm eq}\gamma H}{\rho V}$.

To take into account the harmonic forcing, we write $g^\star = g + a\cos\omega t$, the resulting force (Eq. (12)) is now

$$F^\star(R) \simeq F(R) - \frac{\rho V^2}{\pi R_{\rm eq}^3} a\cos(\omega t)\,. \tag{21}$$

We finally obtain an equation similar to a classical forced solid friction oscillator:

$$\ddot{u} + \omega_1^2 u + \mu sgn(\dot{u}) = A\,\cos(\omega t) \tag{22}$$

with $A = \frac{2}{\rho V}\frac{\rho a V^2}{\pi R_{\rm eq}^3} = \frac{-2\pi S R_{\rm eq}}{\rho V}\frac{a}{g}$.

The dynamics of such oscillators is controlled by the two ratios [28]: $\Lambda = \frac{A}{\mu}$ and $\Omega = \frac{\omega}{\omega_1}$. In the (Ω, Λ)-plane, different regions correspond to particular motion. For $\Lambda < 1$ the line is completely stuck whatever the frequency. For $\Lambda \geq 1$ the line can move and presents stick-slip motion, we have from equation (20) and equation (22): $\Lambda = \frac{(1-\cos\theta_{\rm E})}{H}\frac{a}{g}$. The threshold condition to put the contact line into motion is then given by:

$$\frac{a}{g} > \frac{H}{(1-\cos\theta_{\rm E})} \simeq 0.26\,. \tag{23}$$

This is in quite good agreement with the experimental values for frequencies close to the Type-II resonance (Fig. 12). For frequencies closer to the Type-I resonance, the threshold is lower ($a/g \simeq 0.05$) due to the coupling of Type-I modes which is not included in this model.

A second threshold corresponds to pure slippage motion. In the particular case where $\Omega = 1$, we have pure slippage behavior for $\Lambda \geq \frac{4}{\pi}$, that is

$$\frac{a}{g} > \frac{4H}{\pi(1-\cos\theta_{\rm E})} \simeq 0.32\,. \tag{24}$$

This value is close to the threshold observed.

Further studies are needed to make quantitative comparison for the different frequencies values and to take into account the coupling of Type-I modes.

3.3.3 Other effects

In our system the analogy cannot be drawn far away because of the change in resonance frequency due to the boundary condition effect, and the complex coupling between contact angle oscillation and contact line motion.

In [18], for gas levitation droplet oscillations, the authors described nonlinear effects due to asymmetry in the potential energy of the drop for larger and smaller radius than the equilibrium radius. Equation (11) shows clearly the nonharmonicity of the potential. These effects also induce changes in resonance frequencies and influence the dynamics.

The viscous dissipation in the edge near the contact line may explain the deviation between dynamic and static contact angles, as shown in Figure 11.

4 Conclusion

We study the mechanical forcing of a sessile flattened drop of water on a polystyrene substrate. At low excitation amplitude, the drops present axisymmetric modes of oscillations with a pinned contact line condition, as long as the contact angle variations belong to the interval $[\theta_{\rm r}, \theta_{\rm a}]$. The oscillations are linear, and their spectra exhibit a set of discrete resonance frequencies, depending on the drop size. These modes can be interpreted with a simple model: 1D approximate stationary-waves conditions coupled to the dispersion relation of capillary-gravity waves. The theoretical results are in good agreement with experimental data.

In a second part of the work, at a higher-amplitude regime, above an acceleration threshold depending on drop size and frequency, we observe nonlinear oscillations of the drop radius. These behaviors have strong analogies with forced dry friction oscillators, we observe for instance stick-slip motion of the contact line at moderate forcing amplitude.

By measuring response spectra at constant acceleration as for the pinned modes, we find that in certain frequency regions the contact line remains completely stuck. This feature is original and due to the finite size of the drop. In immersed plate experiments, due to infinite extension of the interface, such behavior cannot be observed: there is no selection of frequencies due to stationary-wave conditions. In regions close to resonance of pinned modes, the radius oscillation amplitude is larger and presents resonance peaks, which are enlarged and shifted to lower frequencies as the excitation amplitude is increased. This can be explained by a modification of the boundary conditions at the contact line for the surface waves. Using the same model as in the first part, we find a simple relation between pure moving contact line modes (constant contact angle) and pure pinned contact line modes that gives a good order of the frequency shift.

Another application of our study using vertical vibrations is to facilitate the motion of droplets under an external field (gravity, chemical gradients...). We have shown that the line is no longer pinned above a threshold acceleration, where drops are free to move. Here we avoided it using a slightly concave substrate, but it can be very interesting for practical uses.

In a forthcoming publication, we shall describe nonaxisymmetric modes of the contact line, which show up at higher acceleration.

References

1. H. Lamb, *Hydrodynamics* (Cambridge University Press, 1932).
2. C. Bisch, A. Lasek, H. Rodot, J. Mec. Theor. Appl. **1**, 165 (1982).
3. M. Strani, F. Sabetta, J. Fluid Mech. **141**, 233 (1984).
4. Y. Watanabe, Jpn. J. Appl. Phys. **24**, 351 (1985).
5. T. Tsukada, M. Sato, N. Imaishi, *et al.*, J. Chem. Eng. Jpn. **20**, 88 (1987).
6. R.W. Smithwick, J.A.M. Boulet, J. Colloid Interface Sci. **130**, 588 (1988).

7. R.W. Smithwick, D.M. Hembree, J. Colloid Interface Sci. **140**, 57 (1990).
8. D.W. DePaoli, T.C. Scott, O.A. Basaran, Sep. Sci. Technol. **27**, 2071 (1992).
9. O.A. Basaran, D.W. DePaoli, Phys. Fluids **6**, 2923 (1994).
10. E.D. Wilkes *et al.*, Phys. Fluids **9**, 1512 (1997).
11. B. Vukasinovic, A. Glezer, M.K. Smith, Phys. Fluids **12**, (2000) S12.
12. A.J. James, B. Vukasinovic, M.K. Smith *et al.*, J. Fluid Mech. **476**, 1 (2003).
13. A.J. James, M.K. Smith, Ari Glezer, J. Fluid Mech. **476**, 29 (2003).
14. M. Rein, Fluid Dyn. Res. **12**, 61 (1993).
15. V. Bergeron, D. Quere, Phys. World **14**, 27 (2001).
16. D. Richard, D. Quere, Europhys. Lett. **50**, 769 (2000).
17. K. Okumura, F. Chevy, D. Richard, *et al.*, Europhys. Lett. **62**, 237 (2003).
18. M. Perez, L. Salvo, M. Suéry, *et al.*, Phys. Rev. E **61**, 2669 (2000).
19. N.E. Bixler, R.E. Benner, *4th International Conference on Numerical Methods in Laminar and Turbulent Flow* (Pineridge Press, Swansea, 1985) p. 1336.
20. L.M. Hocking, J. Fluid Mech. **179**, 267 (1987).
21. G.W. Young, D. S.H., J. Fluid Mech. **174**, 327 (1987).
22. C.-L. Ting, M. Perlin, J. Fluid Mech. **295**, 263 (1995).
23. C. Andrieu, C. Sykes, F. Brochard, Langmuir **10**, 2077 (1994).
24. M. Fabretto, R. Sedev, J. Ralston, *Proceedings of the Third International Symposium on Contact Angle, Wettability and Adhesion*, edited by K.L. Mittal, Vol. **3** (VSP International Science Publishers, 2003) p. 161.
25. T.S. Meiron, A. Marmur, I.S. Saguy, J. Colloid Interface Sci. **274**, 637 (2004).
26. L. Landau, M. Lifshitz, *Fluid Mechanics*, 2nd edition (Butterworth-Heinemann, 1987).
27. J.F. Joanny, PhD Thesis, University Paris VI, 1985.
28. J.P. Den Hartog, Trans. Am. Soc. Mech. Eng. **53**, 107 (1931).
29. S.W. Shaw, J. Sound Vib. **108**, 305 (1986).
30. H.-K. Hong, C.-S. Liu, J. Sound Vib. **229**, 1171 (2000).
31. Y. Gu, D. Li, Colloids Surfaces A: Physicochem. Eng. Asp. **142**, 243 (1998).